Research Papers

GREENSUSMATER

Greensusmater
Vol. 3, No. 2, 2026, 09
https://doi.org/10.62755/gsm.2026.09

Check for updates

Influence of the Bismuth Precursor on Phase Purity and Photocatalytic Activity of Hydrothermally Synthesised $BiVO_4$ for Dye and Antibiotic Degradation

Rima Nurfitria[1,*], Nadiya Rifqah Kurnia[1], Alex Triputra Lumban Tobing[1]

[1] *Department of Materials Engineering, Faculty of Industrial Technology, Institut Teknologi Sumatera, Terusan Ryacudu, Way Hui, Jati Agung, Lampung Selatan 35365, Indonesia*

Corresponding author: rima.121360012@student.itera.ac.id

ARTICLE HISTORY: Received: July 3, 2026 | Revised: September 24, 2026 | Accepted: September 28, 2026

ABSTRACT

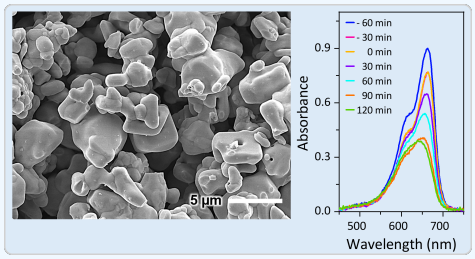

Bismuth vanadate ($BiVO_4$) is widely studied as a visible-light-responsive photocatalyst, but the influence of the bismuth precursor on phase composition and the resulting photocatalytic activity has rarely been quantified. In this work, two $BiVO_4$ samples were synthesised hydrothermally under identical conditions and calcined at 600 °C, differing only in the bismuth source: basic bismuth nitrate $Bi_5O(OH)_9(NO_3)_4$ (BVO–1) and bismuth nitrate pentahydrate $Bi(NO_3)_3{\cdot}5H_2O$ (BVO–2), both with NH_4VO_3 as the vanadium source. Rietveld refinement of X-ray diffraction data shows that BVO–2 is phase-pure monoclinic-scheelite $BiVO_4$ (clinobisvanite), whereas BVO–1 is a three-phase mixture of approximately 25% $BiVO_4$, 59% $Bi_5O_7NO_3$, and 16–19% β-Bi_2O_3. Field-emission scanning electron microscopy is consistent with this finding: BVO–2 forms uniform faceted polyhedra (1–2 µm), while BVO–1 is a heterogeneous aggregate of sub-400 nm particles with at least three coexisting morphologies. X-ray photoelectron spectroscopy of BVO–2 shows single Bi(III) and V(V) states, and diffuse reflectance spectroscopy gives optical band gaps of 2.55 eV for BVO–1 and 2.50 eV for BVO–2. Photocatalytic degradation of methylene blue (MB), methyl orange, tetracycline (TC), and ciprofloxacin under germicidal UV-C irradiation at 253.7 nm reveals a pollutant-dependent activity inversion: BVO–1 outperforms BVO–2 for cationic MB (k=7.6 × 10^{-3} min^{-1} against 3.9 × 10^{-3} min^{-1}) in line with its larger dark adsorption of the dye, whereas BVO–2 is the more active for both antibiotics, with the larger margin for TC (k_{TC}=15.2 × 10^{-3} min^{-1}, 1.8× that of BVO–1). These results identify the bismuth precursor as a determinant of phase purity in the hydrothermal synthesis of $BiVO_4$: $Bi(NO_3)_3{\cdot}5H_2O$ yields phase-pure $BiVO_4$, whereas $Bi_5O(OH)_9(NO_3)_4$ produces a multi-phase composite whose advantage was observed only for MB, where adsorption contributes strongly.

Keywords: *$BiVO_4$; Bismuth Precursor; Hydrothermal Synthesis; Rietveld Refinement; Photocatalysis; Antibiotic Degradation; Methylene Blue; Tetracycline; Ciprofloxacin*

1. INTRODUCTION

Synthetic dyes and antibiotics are among the organic pollutants most frequently detected in surface water and treated effluent, and their persistence through conventional treatment has sustained interest in advanced oxidation processes [1,2]. Heterogeneous photocatalysis is attractive among these because it operates at ambient temperature and pressure and converts the pollutant rather than transferring it to another phase. Semiconductor photocatalysts based on metal oxides and oxysalts, including TiO_2, ZnO, WO_3, and $BiVO_4$, have been studied extensively for this purpose [3,4,5].

Bismuth vanadate ($BiVO_4$) in its monoclinic-scheelite (clinobisvanite) modification has been widely investigated as a visible-light photocatalyst owing to its narrow band gap (≈2.4 eV), suitable band edges for water oxidation and pollutant degradation, low toxicity, and chemical stability under operating conditions [3,4,5]. However, its photocatalytic activity depends strongly on the phase obtained, and the phase in turn is set by the synthesis conditions [6,7]. Hydrothermal synthesis is regarded as a green route because it operates at moderate temperature, in aqueous solvent, and without organic surfactants or templates [6,8].

Despite the maturity of $BiVO_4$ synthesis, the choice of bismuth precursor in hydrothermal protocols is rarely justified or systematically studied, because the precursor is generally treated as an interchangeable source of Bi^{3+} even though the available bismuth nitrates differ in hydrolysis behaviour and in the amount of bismuth delivered per unit mass. The most commonly used precursor is $Bi(NO_3)_3{\cdot}5H_2O$, but other alternatives, most notably the basic bismuth nitrate $Bi_5O(OH)_9(NO_3)_4$ (sometimes labelled "bismuth subnitrate"), are commercially available and have been proposed as lower-cost and lower-toxicity options [9]. Whether these alternative precursors deliver the same phase-pure product after hydrothermal treatment, however, is an open question.

The hydrolysis behaviour of $Bi_5O(OH)_9(NO_3)_4$ under hydrothermal conditions is complex: the oxynitrate framework is comparatively robust and may require energetic conditions to fully release Bi^{3+} for reaction with vanadate. Incomplete decomposition would leave residual bismuth oxynitrate that could persist, or transform further upon subsequent calcination, into phases such as $Bi_5O_7NO_3$ [10,11] or β-Bi_2O_3. The latter is metastable within ≈330–650 °C [12,13], the range in which post-hydrothermal calcination is commonly performed.

In this study we directly compare two hydrothermal

© 2026 The Authors

This article is licensed under CC-BY 4.0 Open Access

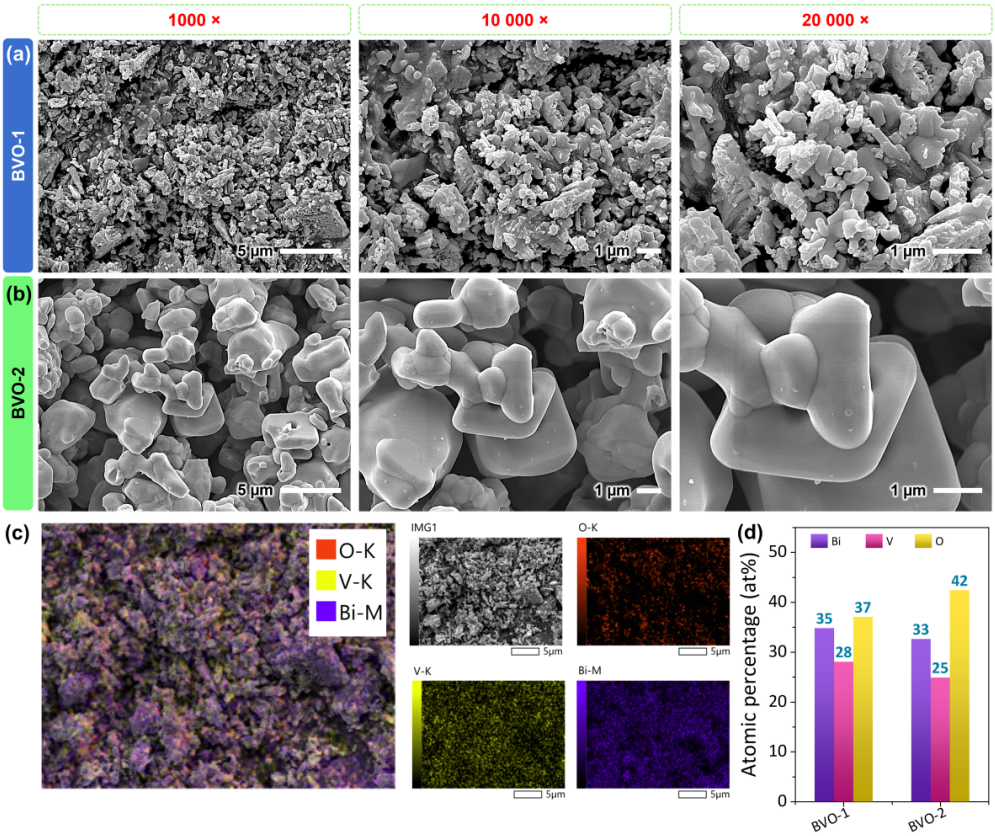

Figure 1. FESEM micrographs and EDS analysis of the two $BiVO_4$ samples. (a) BVO–1 ($Bi_5O(OH)_9(NO_3)_4$ precursor), a heterogeneous aggregate of submicron particles with multiple coexisting morphologies; (b) BVO–2 ($Bi(NO_3)_3{\cdot}5H_2O$ precursor), uniform 1–2 µm faceted polyhedra, both at 1000×, 10000× and 20000× magnification. (c) EDS elemental maps of BVO–1, showing the combined signal and the individual O *K*, V *K* and Bi *M* distributions. (d) EDS atomic percentages of Bi, V and O for the two samples.

$BiVO_4$ preparations that differ only in the bismuth source: $Bi_5O(OH)_9(NO_3)_4$ (BVO–1) versus $Bi(NO_3)_3{\cdot}5H_2O$ (BVO–2). All other parameters (vanadium source, hydrothermal temperature, time, post-calcination at 600 °C) were held identical. Rietveld refinement against multi-phase models is used to quantify the phase composition, and field-emission scanning electron microscopy (FESEM) to characterise the resulting morphology. The photocatalytic activity is benchmarked against four pollutants spanning two dye classes (cationic methylene blue, anionic methyl orange) and two antibiotic classes (tetracycline, ciprofloxacin). The central question is whether precursor choice alone can determine phase purity and photocatalytic performance, and whether the resulting trade-offs between surface adsorption and intrinsic photoactivity favour one precursor for a broad pollutant scope.

2. MATERIALS AND METHODS

2.1 Materials

Basic bismuth nitrate $Bi_5O(OH)_9(NO_3)_4$ ("bismutum subnitricum", ≥98%, Merck 101878) and bismuth(III) nitrate pentahydrate $Bi(NO_3)_3{\cdot}5H_2O$ (reagent grade, crystals, ≥98%, Sigma-Aldrich 248592) were used as bismuth sources for samples BVO–1 and BVO–2, respectively. Ammonium metavanadate NH_4VO_3 (ACS reagent, ≥99.0%, Sigma-Aldrich), methylene blue, methyl orange, tetracycline hydrochloride, and ciprofloxacin (analytical grade) were used as received. Deionised water was used throughout.

2.2 Hydrothermal Synthesis and Calcination

The synthesis followed a recently reported hydrothermal protocol [14] with the bismuth source as the sole variable. In a typical preparation, 2.9 g of the bismuth precursor was dissolved in 50 mL of deionised water under continuous stirring. Separately, 0.70 g of NH_4VO_3 was dissolved in 30 mL of deionised water and heated to 60 °C until fully dissolved. The vanadium solution was added dropwise to the bismuth solution and the mixture was stirred for 30 min. The resulting yellow suspension was transferred into a Teflon-lined stainless-steel autoclave, sealed, and held at 150 °C for 24 h. After natural cooling to room temperature, the solid was recovered by vacuum filtration, rinsed thoroughly with deionised water, and dried in an oven at 80 °C for 2 h. The dried powder was subsequently calcined in static air at 600 °C for 2 h (heating rate 5 °C/min). The two products are designated BVO–1 (Bi precursor $Bi_5O(OH)_9(NO_3)_4$) and BVO–2 (Bi precursor $Bi(NO_3)_3{\cdot}5H_2O$). Because the two bismuth sources differ in molar mass, the fixed precursor mass of 2.9 g corresponds to different Bi/V molar ratios. The 0.70 g of NH_4VO_3 provides 5.98 mmol of vanadium in both preparations, whereas the bismuth charged is 5.98 mmol for $Bi(NO_3)_3{\cdot}5H_2O$ (M=485.07 g/mol) and 9.92 mmol for $Bi_5O(OH)_9(NO_3)_4$ (M=1461.98 g/mol). The Bi/V molar ratio is therefore 1.00 for BVO–2 and 1.66 for BVO–1, so the BVO–1 preparation carries a bismuth excess of approximately 66%.

© 2026 The Authors | CC-BY 4.0

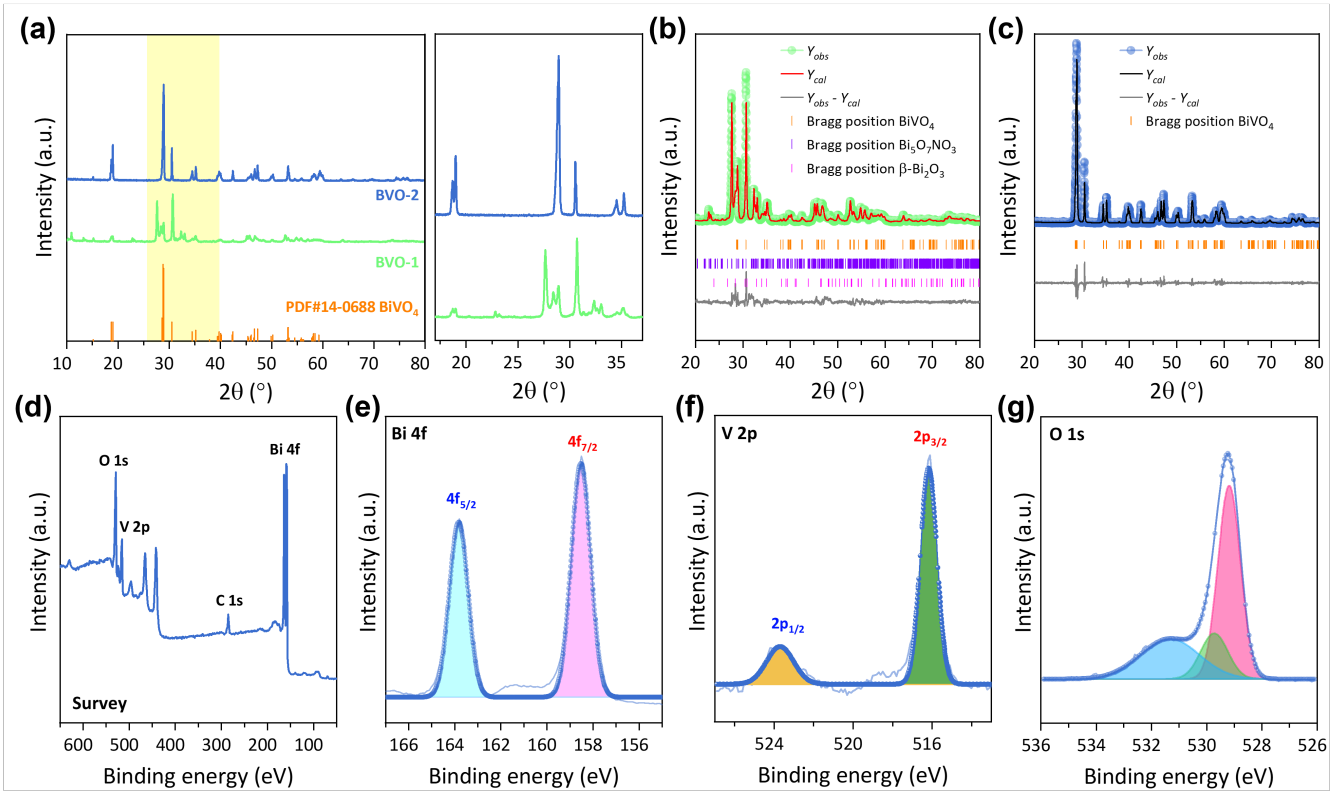

Figure 2. XRD and XPS characterisation of the two $BiVO_4$ samples. (a) Overlaid XRD patterns of BVO–1 and BVO–2 with the PDF 00–014–0688 ms-$BiVO_4$ reference, plotted from 10° 2θ, the window common to both measurements (right: an enlarged view of the region containing the additional reflections). (b) Three-phase Rietveld refinement of BVO–1 (ms-$BiVO_4$ + $Bi_5O_7NO_3$ + β-Bi_2O_3) and (c) single-phase refinement of BVO–2 (ms-$BiVO_4$); each shows Y_{obs}, Y_{cal}, the residual $Y_{obs}-Y_{cal}$, and Bragg-tick positions. (d–g) XPS of BVO–2, with binding energies referenced to adventitious carbon at 284.8 eV: (d) survey spectrum; (e) Bi 4f, the two shaded peaks being the $4f_{7/2}$ and $4f_{5/2}$ components of a single Bi(III) spin-orbit doublet; (f) V 2p, likewise a single V(V) doublet; and (g) O 1s, resolved into lattice oxygen at 529.5 eV and a broader surface component at 531.4 eV. Circles are the measured intensity and the solid line the fitted envelope.

2.3 Characterisation

The crystalline structure and phase composition were analysed by X-ray diffraction (XRD) on a Rigaku SmartLab SE Basic diffractometer with Cu Kα radiation (λ = 1.5406 Å), scanned over 5–80° 2θ for BVO–1 and 10–80° 2θ for BVO–2, at a step of 0.01°; each pattern was refined over its full measured range, and the two are compared from 10° 2θ, the window common to both measurements. Rietveld refinement was carried out in BGMN v4.2.22 through the Profex 5 interface [15,16] against the ICDD structure models of clinobisvanite ms-$BiVO_4$ (PDF 00–014–0688), $Bi_5O_7NO_3$ (PDF 00–051–0525), and β-Bi_2O_3 (PDF 00–027–0050, Harwig 1977). The morphology was examined by field-emission scanning electron microscopy (FESEM) on a JEOL JSM-IT700HR operated at 10 kV, and the average particle size was determined by image analysis (ImageJ; $n \geq 120$ particles per sample). Energy-dispersive X-ray spectroscopy (EDS) maps and standardless ZAF quantification were acquired on the same instrument at 10 kV (live time 30 s) with oxygen quantified directly; the limitations of these conditions are set out in Section 3. X-ray photoelectron spectroscopy (XPS, Kratos Axis Supra, monochromatic Al Kα) was used to determine the chemical states of Bi, V, and O in BVO–2; binding energies were referenced to C 1s at 284.8 eV, and the spectra were fitted with pseudo-Voigt line shapes on a Shirley background. Diffuse reflectance spectra (Shimadzu UV-2600i Plus, integrating sphere, 190–800 nm) were converted to the Kubelka–Munk function $F(R)$, and the optical band gap was obtained from the Tauc plot of $(F(R)h\nu)^2$ against photon energy for a direct allowed transition.

2.4 Photocatalytic Activity Tests

Photocatalytic experiments were performed for four pollutants spanning two chemical classes, the dyes methylene blue (MB, cationic; initial concentration 5 ppm; monitored at 663 nm) and methyl orange (MO, anionic; 5 ppm; 464 nm), and the antibiotics tetracycline hydrochloride (TC; 10 ppm; 357 nm) and ciprofloxacin (CIP; 10 ppm; 271 nm). In each run, 50 mg of catalyst was dispersed in 100 mL of pollutant solution (catalyst loading 0.5 g/L). The suspension was stirred in the dark for 60 min to establish adsorption-desorption equilibrium, with aliquots withdrawn at t=−60 min, −30 min, and 0 min. The illumination phase was initiated at t=0 min using four 10 W Philips TUV germicidal lamps emitting at 253.7 nm (UV-C) [17]. This source was selected so that both samples are excited above the absorption edge of every phase present, which allows the two catalysts to be compared under identical illumination. No measurements were performed under visible light, so the activities reported here describe behaviour under UV-C only. Aliquots (3 mL) were collected at 30 min intervals up to 120 min of illumination, filtered, and analysed by UV-Vis spectrophotometry (Shimadzu UV-1900) at the

© 2026 The Authors | CC-BY 4.0

Table 1. Rietveld refinement results for BVO–1 (three-phase: clinobisvanite + $Bi_5O_7NO_3$ + β-Bi_2O_3) and BVO–2 (single-phase clinobisvanite). Uncertainties on the phase fractions are the estimated standard deviations of the refinement and are statistical lower bounds, as discussed in the text.

	BVO–1	BVO–2
Clinobisvanite, ms-$BiVO_4$		
a (Å)	5.1817	5.1999
b (Å)	5.1105	5.0987
c (Å)	11.6754	11.7078
γ (°)	89.791	90.375
phase fraction (wt%)	25.4 ± 0.4	100
$Bi_5O_7NO_3$		
a (Å)	8.5864	–
b (Å)	23.3110	–
c (Å)	5.5383	–
β (°)	108.527	–
phase fraction (wt%)	58.7 ± 0.3	0
β-Bi_2O_3		
a (Å)	7.4493	–
c (Å)	5.8563	–
phase fraction (wt%)	15.9 ± 0.3	0
Refinement quality		
R_{wp} (%)	14.15	12.44
R_{exp} (%)	6.49	8.71
χ^2	4.75	2.04
GoF	2.18	1.43

pollutant-specific monitoring wavelength. The conversions reported below therefore describe the loss of the monitored absorbance band of the parent pollutant. The apparent rate constant k was extracted from the Langmuir–Hinshelwood pseudo-first-order kinetic model (Equation (1)):

$$\ln\left(\frac{C_0}{C}\right) = k\,t, \tag{1}$$

where C_0 and C are the pollutant concentrations, taken proportional to the absorbance at the monitoring wavelength, at t=0 (end of dark adsorption) and at illumination time t, respectively. The apparent rate constant k was obtained by linear regression of $\ln(C_0/C)$ over the illumination phase (t= 0–120 min).

3. RESULTS AND DISCUSSION

3.1 Phase Composition and Morphology

Two $BiVO_4$ samples were prepared under identical hydrothermal and calcination conditions from the two bismuth precursors and are designated BVO–1 ($Bi_5O(OH)_9(NO_3)_4$) and BVO–2 ($Bi(NO_3)_3{\cdot}5H_2O$). Their morphology, phase composition, surface chemical states and optical absorption were examined first, prior to the evaluation of their photocatalytic performance.

The phase composition of the two samples was examined by X-ray diffraction, and the patterns are compared in Figure 2a. The XRD pattern of BVO–2 exhibits sharp, well-defined reflections that can be indexed in full to the monoclinic-scheelite phase of $BiVO_4$ (clinobisvanite, PDF 00–014–0688), with no additional reflections, indicating the formation of phase-pure $BiVO_4$. In contrast, the pattern of BVO–1 contains, in addition to the clinobisvanite reflections, extra intensity near $2\theta \approx 28°$ that cannot be accommodated by ms-$BiVO_4$ alone [18], indicating the coexistence of additional crystalline phases.

To quantify the phase composition, the XRD data were analysed by Rietveld refinement; the refined patterns are shown in Figure 2b,c, and the corresponding lattice parameters, phase fractions, and reliability factors are summarised in Table 1. For BVO–2, the single-phase refinement (Figure 2c) shows a good agreement between the observed (Y_{obs}) and calculated (Y_{cal}) profiles, converging to R_{wp}=12.44 lattice parameters a=5.1999 Å, b=5.0987 Å, c=11.7078 Å, and γ=90.375°, indicating phase-pure clinobisvanite within the detection limit of the method. For BVO–1, a two-phase model (ms-$BiVO_4$ + $Bi_5O_7NO_3$) reduces R_{wp} to ≈18 (≈28-σ) residual peak at 2θ=28.4°. Candidate third phases, namely pucherite (o-$BiVO_4$), α-Bi_2O_3, and $Bi_6O_8(OH)_4(NO_3)_6$, were each tested and refined to zero weight fraction. The inclusion of β-Bi_2O_3 (Harwig 1977) accounts for the residual peak and lowers R_{wp} to 14.15% and χ^2 to 4.75 (Figure 2b). The refined composition of BVO–1 is therefore approximately 25% ms-$BiVO_4$, 59% $Bi_5O_7NO_3$, and 16–19% β-Bi_2O_3 (Table 1). A parallel refinement with the β-Bi_2O_3 lattice fixed to literature values reproduces a comparable weight fraction (19.2 %, R_{wp}=15.49 supporting the phase assignment independently of any lattice flexibility. The spread between these two refinement strategies, from 15.9% to 19.2%, is an order of magnitude larger than the estimated standard deviations returned by the refinement. Those deviations describe the statistical precision of the fit alone and exclude the systematic contribution of the choice of structural model, so they are treated here as lower bounds on the uncertainty and the phase fractions are quoted accordingly. The phase assignment itself is unaffected, since both strategies require β-Bi_2O_3 to account for the residual intensity at 2θ=28.4°. Overall, the refinement results indicate that $Bi(NO_3)_3{\cdot}5H_2O$ yields single-phase clinobisvanite within the detection limit of the method, whereas $Bi_5O(OH)_9(NO_3)_4$ yields a three-phase product in which $BiVO_4$ accounts for only about a quarter of the mass. The combined morphological and crystallographic evidence is consistent with a two-stage decomposition pathway for BVO–1. In the hydrothermal stage, $Bi_5O(OH)_9(NO_3)_4$ only partially hydrolyses, dehydrating to the oxynitrate framework $Bi_5O_7NO_3$ according to $Bi_5O(OH)_9(NO_3)_4 \rightarrow Bi_5O_7NO_3 + 2\,H_2O + 3\,HNO_3$; in this scheme only about one-fifth of the bismuth reacts with VO_3^-, which would account for the observed ≈25 wt% ms-$BiVO_4$. During subsequent calcination at 600 °C, a portion of the residual $Bi_5O_7NO_3$ undergoes further thermal decomposition. The chosen temperature lies within the metastability window of β-Bi_2O_3 (≈330–650 °C), which favours formation of the β polymorph over the thermodynamically stable α-Bi_2O_3 and is consistent with the Rietveld-refined α:0 wt%, β: 16 to 19 wt% partition. In contrast, $Bi(NO_3)_3{\cdot}5H_2O$ is expected to release Bi^{3+} directly under hydrothermal conditions, which would enable complete reaction with VO_3^-, consistent with the phase-pure ms-$BiVO_4$ obtained. The three coexisting morphologies observed in Figure 1a may be associated with the three quantitatively refined phases: blocky crystallites with ms-$BiVO_4$, small spherical particles with β-Bi_2O_3, and elongated plates or rods with layered $Bi_5O_7NO_3$. This association rests on particle size and habit rather than on a compositional measurement of individual particles.

To probe the surface chemical states of the phase-pure sample, XPS analysis was carried out on BVO–2 (Figure 2d–g). The survey spectrum shows the presence of Bi, V, and O, together with adventitious carbon serving as the reference for calibration (Figure 2d). The high-resolution Bi 4f spectrum re-

© 2026 The Authors | CC-BY 4.0

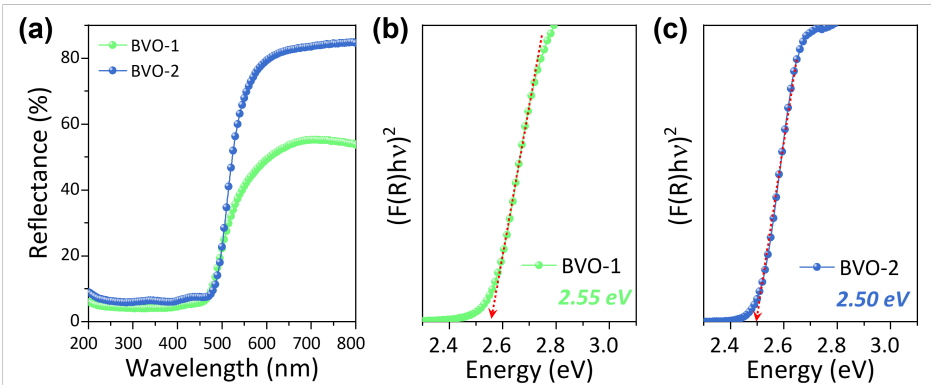

Figure 3. Optical properties of the two $BiVO_4$ samples. (a) Diffuse reflectance spectra of BVO–1 and BVO–2; (b, c) Tauc plots of $(F(R)h\nu)^2$ against photon energy for a direct allowed transition, with the linear extrapolations giving band gaps of 2.55 eV for BVO–1 and 2.50 eV for BVO–2.

veals binding energy peaks at ≈158.7 eV (Bi $4f_{7/2}$) and ≈164.0 eV (Bi $4f_{5/2}$), with a spin-orbit splitting of ≈5.3 eV, characteristic of Bi^{3+} in the $BiVO_4$ lattice [19,20] (Figure 2e). Similarly, the V 2p spectrum shows peaks at ≈516.4 eV (V $2p_{3/2}$) and ≈523.7 eV (V $2p_{1/2}$), consistent with V^{5+} in the vanadate framework, with no evidence of lower oxidation states such as V^{4+} [21,22] (Figure 2f). The O 1s spectrum resolves into two components (Figure 2g): a main peak at ≈529.5 eV, assigned to lattice oxygen in Bi-O and V-O bonds (O_L), and a higher-binding-energy component at ≈531.4 eV, corresponding to chemisorbed oxygen or surface hydroxyl groups (O_C), which together carry approximately 70% and 30% of the O 1s intensity, respectively [22]. The latter component is not assigned to oxygen vacancies, since the C 1s region of the same surface contains C-O and O-C=O contributions and the present data do not separate the two possible origins at this binding energy. Overall, the XPS results indicate that bismuth and vanadium are present as Bi^{3+} and V^{5+}, consistent with the phase-pure clinobisvanite identified above by Rietveld refinement.

The optical absorption of the two samples was compared by diffuse reflectance spectroscopy (Figure 3a). Both samples absorb strongly below about 500 nm and reflect above it, with the reflectance plateau of BVO–1 (about 55%) well below that of BVO–2 (about 85%). The Tauc plots for a direct allowed transition (Figure 3b,c) give optical band gaps of 2.55 eV for BVO–1 and 2.50 eV for BVO–2. The value for BVO–2 lies within the 2.4–2.5 eV range reported for monoclinic $BiVO_4$ [7,19]. The two edges are close, and the difference of 0.05 eV is comparable to the uncertainty of the extrapolation, so it is not interpreted here beyond noting that its direction is the one expected from the wider-gap $Bi_5O_7NO_3$ and β-Bi_2O_3 phases present in BVO–1. Both edges lie far below the 4.88 eV photon energy of the UV-C source used in the photocatalytic tests, so photon harvesting is not expected to limit either sample. Overall, the two precursors give products that differ in phase composition and primary particle size but not appreciably in optical absorption edge, and these differences are expected to influence their photocatalytic behaviour.

The FESEM micrographs in Figure 1(a,b) show that the morphology differs between the two products. BVO–1 (Figure 1a), prepared from $Bi_5O(OH)_9(NO_3)_4$, appears as a heterogeneous aggregate of small particles (≈100–400 nm) in which at least three distinguishable morphologies coexist: faceted blocky crystallites 200–400 nm in size, small spherical features 30–50 nm, and elongated rod- or plate-like fragments. How these habits relate to the phases identified below is considered after the diffraction results. BVO–2 (Figure 1b), prepared from $Bi(NO_3)_3{\cdot}5H_2O$, is, by contrast, uniform: it consists of faceted polyhedral crystallites ≈1–2 µm in size with little aggregation. ImageJ analysis of the 20 000× frames yields a mean equivalent diameter of 200 nm for BVO–1 and 1.2 µm for BVO–2, about six times smaller for the multi-phase product, a size difference that is relevant to the interpretation of the photocatalytic data discussed below. Elemental analysis by EDS detected only bismuth, vanadium and oxygen in both samples. The elemental maps acquired for BVO–1 (Figure 1c) show bismuth, vanadium and oxygen distributed uniformly across the imaged field, with no regions of segregation resolvable at this magnification, and the atomic percentages obtained for the two samples are compared in Figure 1d. These percentages are semi-quantitative and are reported for the elements present and their distribution rather than for composition. At a landing voltage of 10 kV the overvoltage of the vanadium *K* line is only 1.83, bismuth is quantified on its *M* lines, and the vanadium *Lα* and oxygen *Kα* lines are separated by 14 eV, well below the resolution of the detector in that range. The composition of the two samples is therefore taken from the charged stoichiometry and from the diffraction analysis that follows.

3.2 Photocatalytic Activity

The photocatalytic performance of BVO–1 and BVO–2 was benchmarked against four pollutants representing two dye classes (Figure 4: top row methylene blue, MB; bottom row methyl orange, MO) and two antibiotic classes (Figure 5: top row ciprofloxacin, CIP; bottom row tetracycline, TC). These pollutants were selected as model contaminants because of their widespread occurrence in textile and pharmaceutical wastewater and their persistence in aquatic environments. Each test comprised 60 min of stirring in the dark to establish adsorption-desorption equilibrium, followed by 120 min of UV-C irradiation. For each pollutant, panels a, b, e and f show the time-evolved UV-Vis spectra over BVO–1 and BVO–2, panels c and g the normalised C/C_0 profile across the dark-adsorption and illumination stages, and panels d and h the pseudo-first-order linearisation $\ln(C_0/C)$ versus t (Equation (1)). The apparent rate constants k and the corresponding linear-fit R^2 are shown directly on each kinetic panel. A pollutant-dependent reversal in activity is observed. Methylene blue, the only cationic pollutant tested, is degraded more

© 2026 The Authors | CC-BY 4.0

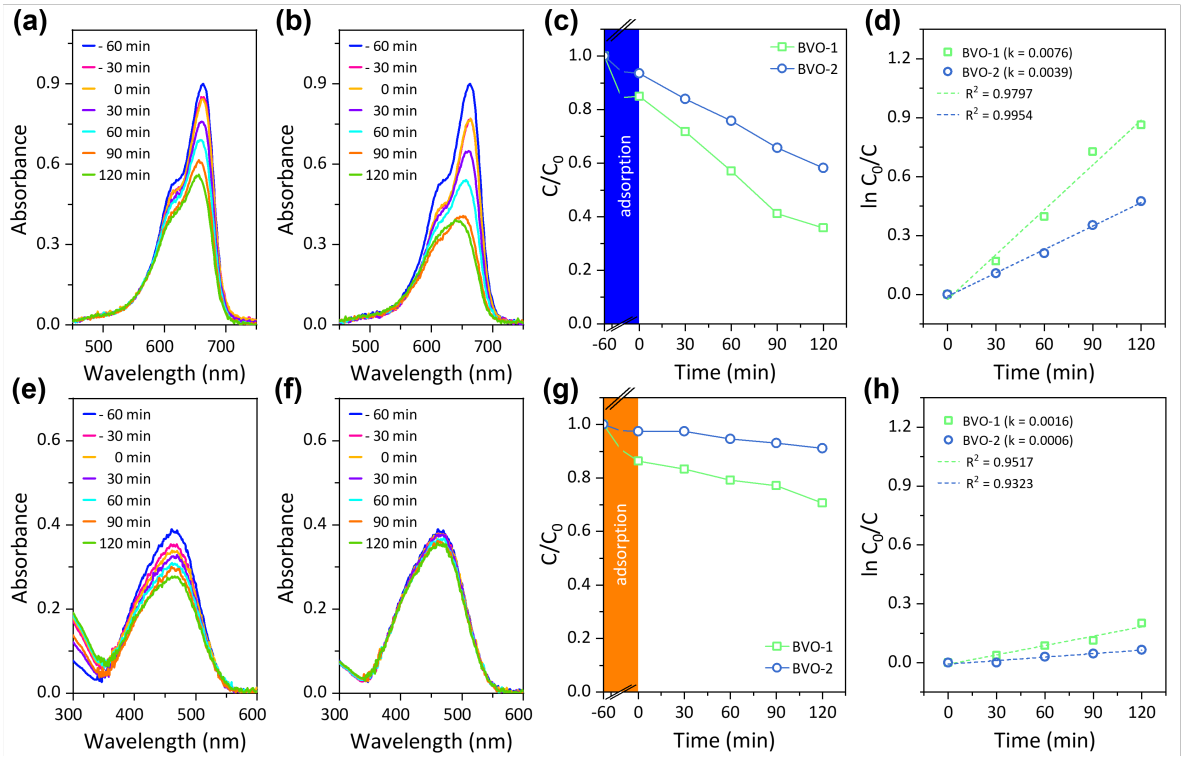

Figure 4. Photocatalytic degradation of dyes under UV-C: methylene blue (MB, cationic, 5 ppm; a–d) and methyl orange (MO, anionic, 5 ppm; e–h). UV-Vis spectra over BVO–1 (a, e) and BVO–2 (b, f); normalised C/C_0 profiles (c, g; 60 min dark then 120 min UV-C); and pseudo-first-order fits $\ln(C_0/C)$ versus t (d, h, Equation (1)) with k and R^2 annotated.

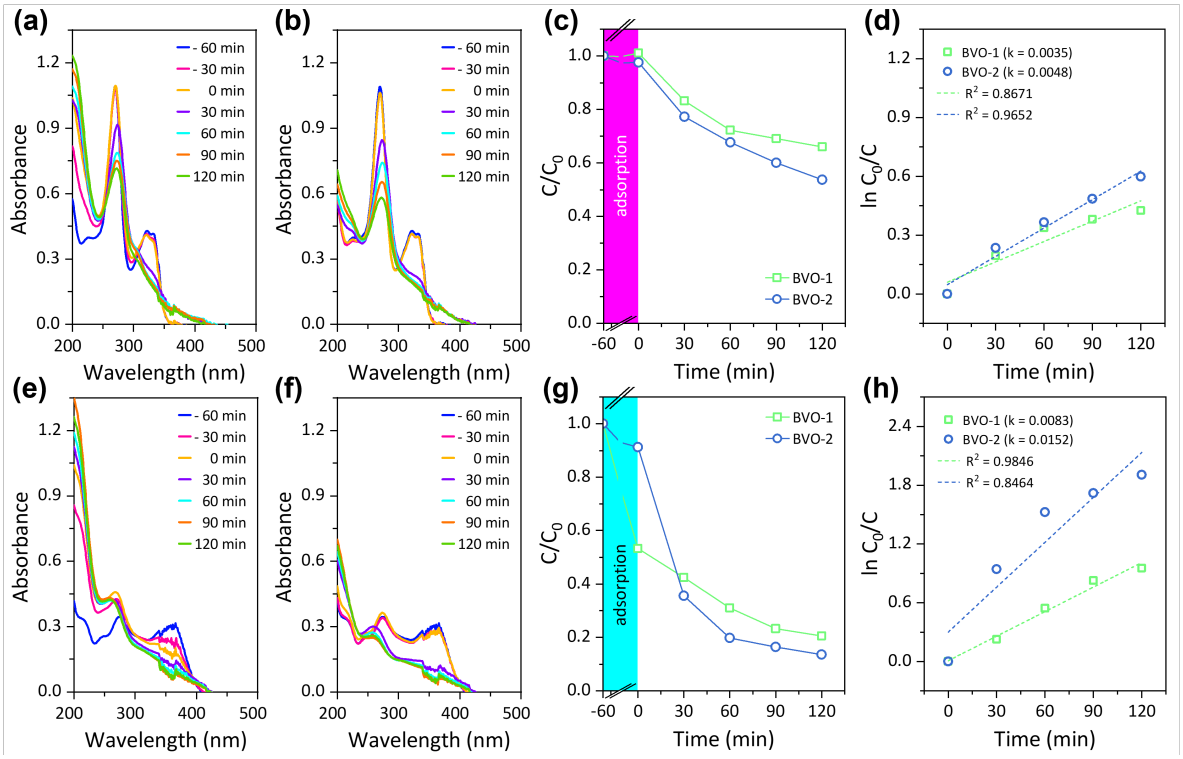

Figure 5. Photocatalytic degradation of antibiotics under UV-C: ciprofloxacin (CIP, 10 ppm; a–d) and tetracycline hydrochloride (TC, 10 ppm; e–h). UV-Vis spectra over BVO–1 (a, e) and BVO–2 (b, f); normalised C/C_0 profiles (c, g; 60 min dark then 120 min UV-C); and pseudo-first-order fits $\ln(C_0/C)$ versus t (d, h, Equation (1)) with k and R^2 annotated.

© 2026 The Authors | CC-BY 4.0

efficiently by the three-phase BVO–1 (57.8% photodegradation after 120 min of illumination, k_{MB}=7.6 × 10^{-3} min^{-1}, R^2=0.9797) than by phase-pure BVO–2 (37.8%, k=3.9 × 10^{-3} min^{-1}, R^2=0.9954; Figure 4d) [23,24]. BVO–1 shows a larger dark adsorption of MB than BVO–2 (15.0% against 6.4%, visible as the deeper C/C_0 drop at t=0 min in Figure 4c) that is carried over into the illuminated stage. This behaviour is consistent with an electrostatic interaction between cationic MB and the residual oxynitrate and oxide phases ($Bi_5O_7NO_3$ and β-Bi_2O_3) that line the BVO–1 surface [25,26]. Methyl orange, which is anionic, is poorly removed by either sample (7.1% and 6.4% photodegradation, k_{MO}=1.6 × 10^{-3} and 0.6 × 10^{-3} min^{-1} for BVO–1 and BVO–2, respectively; Figure 4h). The limited residual activity would likewise be consistent with electrostatic repulsion of MO^- from a negatively charged photocatalyst surface, and the contrast between the two dyes indicates that surface chemistry, in addition to band structure, governs the accessible substrate scope. This behaviour is reversed for the two antibiotics (Figure 5). For ciprofloxacin, both catalysts perform similarly, with the higher rate constant for BVO–2 (45.0% against 34.7% photodegradation; k_{CIP}=4.8 × 10^{-3} min^{-1} against 3.5 × 10^{-3} min^{-1} for BVO–1; Figure 5d) [22,27]. For tetracycline, the difference is larger: BVO–2 reaches 82.1% photodegradation and k_{TC}=15.2 × 10^{-3} min^{-1}, roughly 1.8× faster than BVO–1 (56.2%, 8.3 × 10^{-3} min^{-1}; Figure 5h) [20,28]. The corresponding C/C_0 profile (Figure 5g) drops to below 0.2 within 120 min for BVO–2 while BVO–1 plateaus near 0.4. Moreover, the larger dark-adsorption capacity of BVO–1 for tetracycline (46.7% against 8.7%) does not translate into higher overall removal under illumination (76.7% against 83.6% total removal relative to the initial concentration), indicating that adsorption is not the rate-limiting step for antibiotic degradation; the origin of the difference is considered below.

The germicidal UV-C illumination at 253.7 nm (4.88 eV) is well above the measured absorption edges of the two samples (Figure 3) and the band gaps of all three phases present in the samples ($BiVO_4$ ≈2.4 eV; β-Bi_2O_3 ≈2.6 eV; $Bi_5O_7NO_3$ ≈3.0 eV), so all three phases can, in principle, be photoactivated under these conditions. The higher activity of BVO–2 for antibiotic degradation is therefore unlikely to originate in photon harvesting, and may instead be attributed to the fate of the photogenerated carriers. The phase-pure, micron-sized ms-$BiVO_4$ grains of BVO–2 are expected to present a low density of grain boundaries; their faceted habit is consistent with the {010} and {110} terminations that are known to segregate photogenerated electrons and holes onto distinct surfaces in monoclinic $BiVO_4$ [19,21]. BVO–1, by contrast, contains a large density of internal interfaces between dissimilar phases that may act as recombination sites rather than as effective Type-II heterojunctions, because the phase boundaries between $BiVO_4$, $Bi_5O_7NO_3$, and β-Bi_2O_3 are neither lattice-matched nor crystallographically aligned. On this interpretation, the more efficient use of the absorbed photons by BVO–2 would compensate for its larger primary particle size when the target is bulk-oxidation-limited, as in antibiotic degradation, which requires sustained •OH attack on multiple aromatic rings [29]. However, no measurement of carrier dynamics was performed in this work. Photoluminescence or electrochemical impedance spectroscopy would be required to establish this mechanism directly, and such measurements are the subject of ongoing work.

Conversely, the MB data are consistent with removal governed largely by adsorption at the catalyst surface, with the higher surface coverage of BVO–1 dominating the overall removal rate. The apparent rate constants reported here are not normalised to specific surface area. Since the primary particle size of BVO–1 is smaller than that of BVO–2 by a factor of about six, a larger specific surface area is expected for the three-phase product, and its contribution to the higher methylene blue removal cannot be separated from that of the phase composition and the associated adsorption behaviour. Overall, the two samples show complementary behaviour: BVO–1 is the more effective for the cationic dye, where adsorption contributes strongly, whereas BVO–2 is the more active for both antibiotics, so the precursor sets not only the phase composition but also the substrate scope of the product.

4. CONCLUSIONS

Two $BiVO_4$ photocatalysts were synthesised hydrothermally under identical conditions from different bismuth precursors and evaluated for the degradation of two dyes and two antibiotics. The choice of bismuth precursor was found to exert a quantifiable influence on the phase composition and photocatalytic behaviour of the product, with neither sample outperforming the other across the whole pollutant scope. $Bi(NO_3)_3{\cdot}5H_2O$ yields phase-pure clinobisvanite $BiVO_4$ with 1–2 µm faceted polyhedra (BVO–2), whereas $Bi_5O(OH)_9(NO_3)_4$ produces a three-phase mixture of 25% $BiVO_4$, 59% $Bi_5O_7NO_3$ and 16–19% β-Bi_2O_3 (BVO–1) with about six-fold smaller primary particles. The secondary phases follow from the charged stoichiometry: the bismuth in excess of the 1:1 ratio of $BiVO_4$ is retained as a bismuth oxynitrate, which on calcination at 600 °C, within the β-Bi_2O_3 metastability window, yields the $Bi_5O_7NO_3$ and β-Bi_2O_3 identified by refinement. Photocatalytic benchmarking against four pollutants under UV-C irradiation reveals a pollutant-dependent activity inversion: BVO–1 removes more of the cationic methylene blue (MB; 57.8% against 37.8% photodegradation), where surface adsorption contributes strongly, whereas BVO–2 is the more active for tetracycline (82.1% against 56.2%) and ciprofloxacin, where adsorption does not limit the rate. Methyl orange is poorly degraded by either catalyst. These findings identify the bismuth precursor as a simple means of tuning the phase composition, morphology, and photocatalytic activity of $BiVO_4$. $Bi(NO_3)_3{\cdot}5H_2O$ is preferable when antibiotic degradation is the objective, whereas $Bi_5O(OH)_9(NO_3)_4$ remains suitable for the removal of MB, the only cationic dye tested here, where a high adsorption capacity is advantageous. Future work should examine whether tuning the calcination temperature to drive $Bi_5O_7NO_3$ to full conversion, or deliberately exploiting the $Bi_5O_7NO_3$/β-Bi_2O_3/$BiVO_4$ composite as an in-built heterojunction, can broaden the substrate scope of the basic-nitrate route.

CREDIT AUTHORSHIP CONTRIBUTION STATEMENT

RN: Conceptualization, Methodology, Investigation, Formal analysis, Visualization, Writing – original draft, Writing – review & editing. **NRK**: Methodology, Investigation, Formal analysis. **ATLT**: Investigation, Resources.

ACKNOWLEDGMENTS

This research did not receive any specific grant from funding agencies in the public, commercial, or not-for-profit sectors.

© 2026 The Authors | CC-BY 4.0

CONFLICT OF INTEREST

The authors declare that they have no known competing financial interests or personal relationships that could have appeared to influence the work reported in this paper.

REFERENCES

[1] Rathi BS, Kumar PS, Vo DN. Critical review on hazardous pollutants in water environment: occurrence, monitoring, fate, removal technologies and risk assessment. *Science of the Total Environment*. 2021;797:149134. doi:10.1016/j.scitotenv.2021.149134.

[2] Ding G, Chen G, Liu Y, Li M, Liu X. Occurrence and risk assessment of fluoroquinolone antibiotics in reclaimed water and receiving groundwater with different replenishment pathways. *Science of the Total Environment*. 2020;738:139802. doi:10.1016/j.scitotenv.2020.139802.

[3] Wang L, Shi X, Jia Y, Cheng H, Wang L, Wang Q. Recent advances in bismuth vanadate-based photocatalysts for photoelectrochemical water splitting. *Chinese Chemical Letters*. 2021;32:1869-1878. doi:10.1016/j.cclet.2020.11.065.

[4] Alijani HQ, Iravani S, Varma RS. Bismuth vanadate (BiVO4) nanostructures: eco-friendly synthesis and their photocatalytic applications. *Catalysts*. 2022;13:59. doi:10.3390/catal13010059.

[5] Orimolade BO, Arotiba OA. Bismuth vanadate in photoelectrocatalytic water treatment systems for the degradation of organics: a review on recent trends. *Journal of Electroanalytical Chemistry*. 2020;878:114724. doi:10.1016/j.jelechem.2020.114724.

[6] Cao X, Gu Y, Tian H, Fang Y, Johnson D, Ren Z, Chen C, Huang Y. Microemulsion synthesis of ms/tz-BiVO4 composites: the effect of pH on crystal structure and photocatalytic performance. *Ceramics International*. 2020;46:20788-20797. doi:10.1016/j.ceramint.2020.05.048.

[7] Dabodiya TS, Selvarasu P, Murugan AV. Tetragonal to monoclinic crystalline phases change of BiVO4 via microwave-hydrothermal reaction: in correlation with visible-light-driven photocatalytic performance. *Inorganic Chemistry*. 2019;58:5096-5110. doi:10.1021/acs.inorgchem.9b00193.

[8] Sajid MM, Amin N, Shad NA, Khan SB, Javed Y, Zhang Z. Hydrothermal fabrication of monoclinic bismuth vanadate (m-BiVO4) nanoparticles for photocatalytic degradation of toxic organic dyes. *Materials Science and Engineering: B*. 2019;242:83-89. doi:10.1016/j.mseb.2019.03.012.

[9] Daminov AS, Yukhin YM, Naydenko ES. Processing of nitrate solutions for the preparation of basic bismuth nitrate and oxide. *Theoretical Foundations of Chemical Engineering*. 2020;54:1020-1025. doi:10.1134/S0040579520050097.

[10] Du X, Wang X. Solution combustion synthesis of Ag-decorated Bi5O7NO3 composites with enhanced photocatalytic properties. *Ceramics International*. 2019;45:1409-1411. doi:10.1016/j.ceramint.2018.09.141.

[11] Zhen Z, Deng Y, Yang H, Sheng Q, Liang T. Facile synthesis of Bi5O7NO3 with enhanced photocatalytic activity by a molten salt strategy and its photocatalytic performance. *Chemical Physics Letters*. 2020;745:137178. doi:10.1016/j.cplett.2020.137178.

[12] Yu N, Liu X, Lu Z, Wang T, Wang J. Polymorph control, phase transitions and photocatalytic activity of bismuth oxide with emphasis on sodium-impurity effects. *Ceramics International*. 2025;51:24960-24969. doi:10.1016/j.ceramint.2025.03.177.

[13] Mishchenko KV, Gerasimov KB, Yukhin YM. Thermal decomposition of some bismuth oxocarboxylates with formation of -Bi2O3. *Materials Today: Proceedings*. 2020;25:391-394. doi:10.1016/j.matpr.2019.12.102.

[14] Kurnia NR, Amanda T, Nurfitria R, Aflaha R, Widakdo J, Rianjanu A. Development and materials characterization of hydrothermally grown niobium-doped BiVO4 for ciprofloxacin and methylene blue degradation. *Greensusmater*. 2025;2:55-61. doi:10.62755/greensusmater.2025.2.2.55-61.

[15] Doebelin N, Kleeberg R. Profex: a graphical user interface for the Rietveld refinement program BGMN. *Journal of Applied Crystallography*. 2015;48:1573-1580. doi:10.1107/S1600576715014685.

[16] Rietveld HM. A profile refinement method for nuclear and magnetic structures. *Journal of Applied Crystallography*. 1969;2:65-71. doi:10.1107/S0021889869006558.

[17] Song K, Mohseni M, Taghipour F. Application of ultraviolet light-emitting diodes (UV-LEDs) for water disinfection: a review. *Water Research*. 2016;94:341-349. doi:10.1016/j.watres.2016.03.003.

[18] Zhu S, Li Q, Huttula M, Li T, Cao W. One-pot hydrothermal synthesis of BiVO4 microspheres with mixed crystal phase and Sm3+-doped BiVO4 for enhanced photocatalytic activity. *Journal of Materials Science*. 2016;52:1679-1693. doi:10.1007/s10853-016-0460-0.

[19] Kamble GS, Ling Y. Solvothermal synthesis of facet-dependent BiVO4 photocatalyst with enhanced visible-light-driven photocatalytic degradation of organic pollutant: assessment of toxicity by zebrafish embryo. *Scientific Reports*. 2020;10:12993. doi:10.1038/s41598-020-69706-4.

[20] Palaniswamy VK, Ramasamy B, Manoharan K, Raman K, Sundaram R. Enhanced photocatalytic degradation of tetracycline antibiotic using m-BiVO4 photocatalyst under visible light irradiation. *Chemical Physics Letters*. 2021;771:138531. doi:10.1016/j.cplett.2021.138531.

[21] Tian H, Wu H, Fang Y, Li R, Huang Y. Hydrothermal synthesis of m-BiVO4/t-BiVO4 heterostructure for organic pollutants degradation: insight into the photocatalytic mechanism of exposed facets from crystalline phase controlling. *Journal of Hazardous Materials*. 2020;399:123159. doi:10.1016/j.jhazmat.2020.123159.

[22] Chen Z, Mi N, Huang L, Wang W, Li C, Teng Y, Gu C. Snow-like BiVO4 with rich oxygen defects for efficient visible light photocatalytic degradation of ciprofloxacin. *Science of the Total Environment*. 2022;808:152083. doi:10.1016/j.scitotenv.2021.152083.

[23] Huang K, Hu T, Wang Y. Enhanced photocatalytic degradation of methylene blue through synthesizing of novel BiVO4/Zn2SnO4 under visible light. *Journal of Solid State Chemistry*. 2021;294:121864. doi:10.1016/j.jssc.2020.121864.

[24] Ranjith R, Karmegam N, Alsawalha M, Hu X, Jothimani K. Construction of g-C3N4/CdS/BiVO4 ternary nanocomposite with enhanced visible-light-driven photocatalytic activity toward methylene blue dye degradation in the aqueous phase. *Journal of Environmental Management*. 2023;330:117132. doi:10.1016/j.jenvman.2022.117132.

[25] Verma S, Rao BT, Singh R, Kaul R. Photocatalytic degradation kinetics of cationic and anionic dyes using Au-ZnO nanorods: role of pH for selective and simultaneous degradation of binary dye mixtures. *Ceramics International*. 2021;47:34751-34764. doi:10.1016/j.ceramint.2021.09.014.

[26] Wang S, Teng F, Zhao Y. Effect of the molecular structure and surface charge of a bismuth catalyst on the adsorption and photocatalytic degradation of dye mixtures. *RSC Advances*. 2015;5:76588-76598. doi:10.1039/c5ra14931b.

[27] Truong HB, Huy BT, Ray SK, Gyawali G, Lee Y, Cho J, Hur J. Magnetic visible-light activated photocatalyst ZnFe2O4/BiVO4/g-C3N4 for decomposition of antibiotic lomefloxacin: photocatalytic mechanism, degradation pathway, and toxicity assessment. *Chemosphere*. 2022;299:134320. doi:10.1016/j.chemosphere.2022.134320.

[28] Hemavibool K, Sansenya T, Nanan S. Enhanced photocatalytic degradation of tetracycline and oxytetracycline antibiotics by BiVO4 photocatalyst under visible light and solar light irradiation. *Antibiotics*. 2022;11:761. doi:10.3390/antibiotics11060761.

[29] Zhang P, Xiao N, Yang L, Liu S, Wang J, Hu J, Tong Z, Zhang G, Ding S, Yu Y. Active species trapping test for the mechanism study of photocatalytic dye degradation: a critical examination. *Applied Catalysis A: General*. 2025;707:120527. doi:10.1016/j.apcata.2025.120527.

© 2026 The Authors | CC-BY 4.0